FINAL REPORT

Development and Applications of Satellite-Based Services

Frank van Graas, Ph.D.
Principal Investigator

August 2000

Avionics Engineering Center
School of Electrical Engineering and Computer Science
Russ College of Engineering and Technology
Ohio University
Athens, Ohio

Prepared under:
Federal Aviation Administration Research Grant 92-G-0023

TABLE OF CONTENTS

LIST OF FIGURES

LIST OF TABLES

EXECUTIVE SUMMARY

The Global Positioning System (GPS) is augmented with reference receivers, at known locations at an airport, and a data broadcast system to improve the accuracy and integrity of GPS to enable aircraft precision approach, landing, and surface movement guidance. The resulting system is referred to as the Local Area Augmentation System (LAAS) Ground Facility (LGF). In support of the development of the LAAS and other satellite-based services, several project were performed under Aviation Research Grant 92-G-0023. These projects can be divided into four major research areas:

- Development and flight testing of prototype LAAS ground and airborne equipment, including high-accuracy simulator testing, analyses of integrity, continuity and availability, and characterization and mitigation of multipath error
- Integration of GPS with a low-cost Inertial Measurement Unit
- LAAS augmentation with an on-airport ranging pseudolite
- Fault detection and exclusion techniques

Major findings of the research are:

1) Feasibility demonstration in October of 1994 of a carrier-smoothed code-phase differential GPS system for Category IIIB (autoland) applications through flight-testing on a Boeing-757 aircraft operated by the United Parcel Service; and
2) Successful flight-test demonstration of a prototype LAAS for Category III landings at the William J. Hughes Technical Center in Atlantic City using FAA's Boeing 727. The architecture of this system forms the basis for the next generation of GPS-based aircraft landing systems.

Other significant findings of the research include:

1) Feasibility demonstration of hybrid DGPS/ILS Glide Slope for aircraft precision approach and landing on a Boeing-757 aircraft.
2) Design and implementation of an integrated multipath-limiting antenna (IMLA) system to significantly reduce the error due to ground multipath.
3) Successful demonstration of the use of the Very-High Frequency (VHF) data broadcast (VDB) system for LAAS.
4) Flight test demonstration of low-cost inertial aiding of differential GPS with coasting time periods of up to two seconds, while maintaining centimeter-level accuracy.
5) Demonstrated feasibility of using a sophisticated simulator to test and characterize high-accuracy differential GPS architectures.
6) Completion of computer models to investigate the availability, integrity and coverage of differential GPS architectures.
7) Completion of a ground multipath model to predict and analyze the effect of earth-surface-based multipath. The model was used to design the IMLA system.

8) Characterization of pseudolite multipath error using an off-frequency pseudolite architecture.
9) First successful integration of an on-airport pseudolite into the LAAS to achieve sub-meter pseudolite ranging accuracy.
10) Major contributions to the development and testing of fault detection and exclusion (FDE) techniques for GPS augmentations, including the development of a baseline FDE algorithm and test procedures.

1.0 INTRODUCTION

The Global Positioning System (GPS) is augmented with reference receivers, at known locations at an airport, and a data broadcast system to improve the accuracy and integrity of GPS to enable aircraft precision approach, landing, and surface movement guidance. The resulting system is referred to as the Local Area Augmentation System (LAAS) Ground Facility (LGF). In support of the development of the LAAS and other satellite-based services, several project were performed under Aviation Research Grant 92-G-0023. These projects can be divided into four major research areas:

1. Development and flight testing of a prototype LAAS, including high-accuracy simulator testing, analyses of integrity, continuity and availability, and characterization of multipath error
2. Integration of GPS with a low-cost Inertial Measurement Unit
3. LAAS augmentation with an on-airport ranging pseudolite
4. Fault detection and exclusion techniques

Each of these research areas is summarized below. Detailed descriptions of these four areas are provided in chapters 2 through 5.

Development and Flight Testing of a Prototype LAAS

The first phase of the development of a prototype LAAS consisted of a carrier-smoothed code phase differential system to determine the feasibility of a robust differential GPS (DGPS) techniques for aircraft precision approach and landing. This system was successfully flight-tested in October of 1994 with a Boeing-757 operated by the United Parcel Service. A total of 50 successful automatic landings were performed at the William J. Hughes Technical Center (WJHTC) in Atlantic City, NJ. This flight test experiment was repeated in early 1995 with similar results as those obtained in 1994. The flight test findings were presented to the International Civil Aviation Organization (ICAO) in early 1995 in Montreal, which resulted in the adoption of differential GPS by ICAO. [1 - 4]

During the 1995 flight tests, the feasibility of hybrid DGPS/ILS was also investigated. To support this test, a hybrid system was designed and implemented. Vertical aircraft guidance was provided by the ILS Glide Slope element, while horizontal guidance was provided by DGPS. Guidance was then provided to the Boeing-757 autoland system through an experimental ARINC-429 interface, specially designed for this test. It was concluded that hybrid DGPS/ILS is feasible for aircraft autoland operations. [4]

The next phase of the development focused on improving the integrity design of the LAAS. This resulted in the implementation of an integrated multipath-limiting antenna system (IMLA) that consists of a 14-element dipole array antenna and a helibowl high-zenith antenna. GPS receivers with two radio frequency (RF) front-ends are connected to each IMLA. In addition, integrity processing algorithms were developed to detect and

exclude errors from one of the IMLA sites. The resulting prototype LAAS was successfully flight-tested in 1997 using FAA's Boeing-727 at the WJHTC. [5 - 10]

A major component of the prototype LAAS is the Very-High Frequency (VHF) data broadcast (VDB) system. Research in this area was focused on analyzing the performance of VDB transmitter/receiver pairs using the Ohio University data broadcast message format. Performance parameters to be characterized included band capacity, coverage, and service volume considerations. [11]

Simulators play an important role in the characterization and certification of landing systems. The satellite simulator test (SST) facilities at the Naval Command, Control and Ocean Surveillance Center (NCCOSC) Research, Development, Test and Engineering Division Detachment Warminster (NRaD) Central Engineering Activity (CEA) laboratory was used to design simulator tests to evaluate differential GPS architectures. Ohio University provided technical assistance in the operation of a differential GPS system during simulator tests, including data analysis, and analyses resulting in proposed simulator improvements. [13]

Computer models are required to evaluate satellite-based system architectures for aircraft precision landing. Such a model will allow for the assessment of the impact of satellite failure scenarios and will characterize the service in terms of reliability, availability, integrity, and coverage. Several models were developed that were used throughout the design of the prototype LAAS. [8, 14 - 16]

Multipath is the dominant error source for satellite-based landing systems. A validated multipath model is required to evaluate different system architectures and to guarantee the accuracy and safety of a satellite-based landing system. In addition, characterization of multipath error is necessary to understand the trade-offs in multipath mitigation. A preliminary ground multipath model was completed and the results from this model were used in the design of the integrated multipath-limiting antenna system. [14, 17]

Integration of GPS with a low-cost Inertial Measurement Unit

A second research topic, focused on general aviation applications, was the characterization of low-cost inertial measurement unit (IMU) aiding of differential GPS. Specifically, IMU aiding was analyzed for cycle slip detection/correction and short-term coasting during approach and landing. The IMU was also investigated as a source for attitude and heading data required for position comparisons between antennas and post-flight data analysis. [12]

LAAS Augmentation with an On-Airport Ranging Pseudolite

Different pseudolite architectures were considered for LAAS augmentation to increase availability of the landing service, while maintaining accuracy and integrity as achieved without the pseudolite. Major design challenges are the development of a pseudolite transmit antenna, reception of the pseudolite signal through a top-mounted aircraft

antenna, and mitigation of the near/far problem. The latter problem was addressed through consideration of pulsed and off-frequency pseudolite architectures. [18 - 20]

Fault Detection and Exclusion Techniques

Fault detection and exclusion algorithms and test methods are important for all GPS augmentations. Research in this area was focused on: 1) The integrity working group of RTCA, Inc. Special Committee 159; and 2) integrity design of the LAAS. A baseline fault detection and exclusion (FDE) algorithm was developed as well as numerous test procedures. Trade studies were performed to determine the appropriate balance between exhaustive off-line testing of software modules, versus limited on-line testing using dedicated equipment suites. [14, 16, 21 - 23]

2.0 PROTOTYPE LAAS FLIGHT TEST EXPERIMENT

The Federal Aviation Administration (FAA) has been aggressively pursuing the use of carrier-smoothed code-phase differential GPS (DGPS) methods for a Local Area Augmentation System (LAAS). A LAAS architecture was developed in 1996 by the FAA LAAS Program Office, with contributions from The MITRE Corporation, Ohio University, Stanford University, and the William J. Hughes Technical Center. Following presentations of the proposed architecture to the FAA Satellite Operational Implementation Team (SOIT) and the Air Transport Association (ATA), the architecture was presented to RTCA, Inc. Special Committee 159, Working Group 4. After some modifications, consensus was reached on the LAAS architecture. In February of 1997, the FAA/RTCA LAAS architecture was proposed and recommended for adoption at the International Civil Aviation Organization (ICAO) Global Navigation Satellite System Panel (GNSSP) Working Group meeting in Gold Coast, Australia. [24]

The LAAS architecture is designed for Category I through Category III precision approach and landing service, and to support surface navigation. A Category III LAAS ground facility consists of four reference elements. Pseudolites are the preferred augmentation to further increase LAAS availability beyond that provided by the GPS satellite constellation. Pseudolite considerations are provided in [18 – 20, 24].

Numerous flight tests were conducted by the FAA during the last several years to demonstrate the feasibility of DGPS for precision approach and landing. [3] The purpose of the flight tests are to demonstrate three key elements of the proposed LAAS architecture: 1) the use of multipath-limiting ground station antennas; 2) the implementation of integrity equations; and 3) the use of the VHF Data Broadcast (VDB). The VDB is a time-division, multiple access (TDMA) broadcast signal specifically designed for ground-to-air data communications using frequencies in the VHF Omnidirectional Range (VOR) band.

The next section provides an overview of the equipment used for the flight tests. This is followed by a description of the multipath-limiting antenna system and a brief section on the implementation of the integrity equations. Next, the flight tests are described and flight test results are provided.

2.1 LAAS Equipment Description

The LAAS architecture is designed to operate using carrier-smoothed C/A-code differential GPS. During previous flight tests, accuracies on the order of 1.1 m (95% vertical) were achieved; but, this did not leave enough margin for achieving integrity with high availability [3]. It was determined that multipath reflections from the ground are the dominant error source when data from multiple ground reference antennas are compared for achieving integrity. After the investigation of several multipath mitigation techniques, multipath-limiting antennas (MLA) were selected for the FAA LAAS architecture.

Figure 2-1 shows a block diagram of the Ground Subsystem used for the flight tests. Differential corrections are calculated for three reference antenna systems. A reference

antenna system consists of a vertical dipole-array antenna and a high-zenith antenna. Each antenna is connected to a narrow-correlator GPS receiver. In the current hardware implementation, two GPS receivers are connected to the same clock. The common clock allows for the evaluation of hardware delays between the two receivers and is also used for pseudolite tests. [18] It is noted that the common clock is not a requirement for the LAAS architecture.

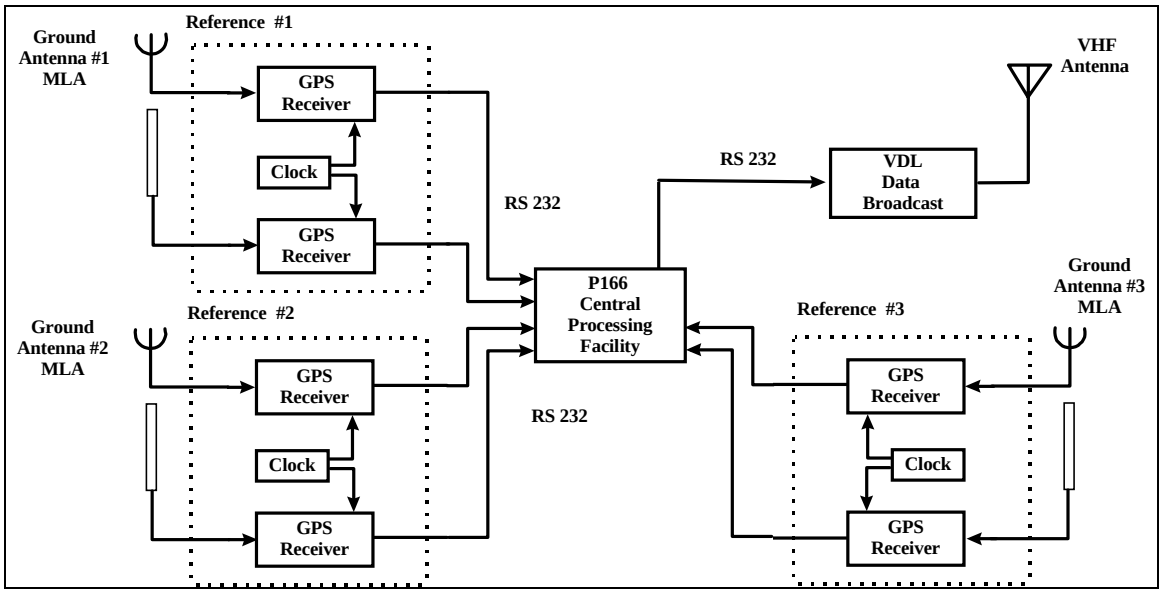

Figure 2-1. Ground Subsystem Block Diagram

All GPS data are collected and processed by a 166 MHz Pentium Processor. The approved differential corrections for each satellite are averaged among the references to increase accuracy. Differential correction data and integrity information are broadcast to the aircraft using the VHF Data Broadcast (VDB) at an FAA-approved frequency of 112.15 MHz. The VDB uses a time-division, multiple-access (TDMA) structure with differential 8-phase shift keyed (D8PSK) modulation. Eight time slots are available, which repeat every 0.5 s. Each time slot accommodates 222 bytes of application data. One VDB time-slot is used to transmit all differential corrections, accumulated Doppler shifts, and integrity information. Flight test results for the VDB system are provided in [11].

The block diagram of the Aircraft Subsystem is shown in Figure 2-2. Two GPS receivers are used to detect receiver hardware failures. These two GPS receivers are interfaced with a 166 MHz Pentium processor, which is also connected to the VDB receiver. Differential GPS position, velocity and integrity information are sent over a serial data bus to the FAA data collection and area navigation (RNAV) system. The RNAV system is capable of driving the cockpit display and autopilot of the FAA Boeing 727. Again, the common clock for the two GPS receivers is not a required element of the LAAS architecture.

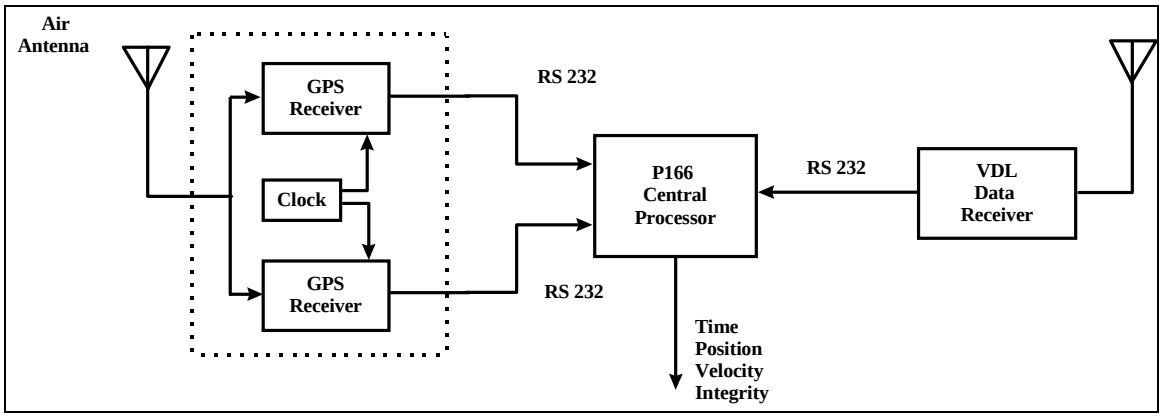

Figure 2-2. Aircraft Subsystem Block Diagram

2.2 Multipath-Limiting Antenna System

Ground multipath was determined to be the dominant error source at the LAAS reference sites. The ground surface and the wet layer below the surface are both large and potentially smooth surfaces from which strong reflections can be sustained for long periods of time. [17] Since these reflections can be present much longer than a typical 100-second C/A-code smoothing period, the resulting multipath error is bias-like over the duration of an aircraft approach.

To achieve the currently proposed LAAS signal-in-space accuracy, continuity and integrity requirements with a service availability of 0.999 or better, it is desirable to limit the ground multipath error to ±0.2 m on each pseudorange measurement. [26] It is further noted that the multipath-limiting technique must work for satellites with a low signal strength down to elevation angles of 5 deg in most operational environments.

Several multipath-limiting techniques were considered, including antenna techniques, GPS receiver measurement processing methods, and post-measurement techniques. [27] It was determined that all currently known measurement processing techniques do not work well at the low signal-to-noise ratios experienced with low-elevation satellites, especially for short-path-delay multipath signals. Therefore, the focus of investigation was turned to the receiving antenna.

The concept for limiting ground-multipath error is based on the fact that ground reflections enter the antenna from negative angles with respect to the local horizontal. An antenna would limit ground-multipath error if the antenna gain for negative elevation angles were smaller than that for the corresponding positive elevation angles. Consider the multipath error envelope for a 0.1-chip spacing correlator shown in Figure 2-3. [28]

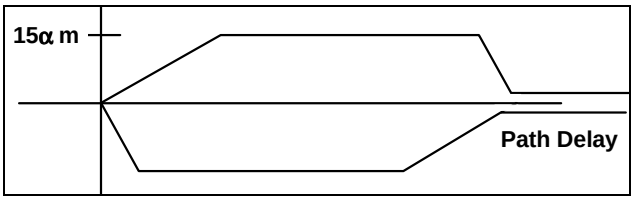

Figure 2-3. Multipath Error Envelope Example for a 0.1-Chip Spacing Correlator.

In Figure 2-3, α is the ratio of the antenna gains for the reflected and the direct GPS signals. For example, if $\alpha < 0.01$, then the multipath error would be less than ±0.15 m. This corresponds to an antenna gain of -40 dB for negative elevation angles relative to their mirrored positive elevation angles. The latter example assumes a reflection coefficient of unit magnitude and a perfectly smooth ground. In an operational environment, the magnitude of the reflection coefficient is less than unity, which allows for the use of an antenna gain of approximately -35 dB for reflected versus direct GPS signals. Furthermore, as the satellite elevation angle increases, the reflection coefficient decreases. This allows the use of less rejection in the antenna gain pattern for higher elevation angles.

The antenna design for the LAAS is based on the use of two antennas to achieve the -35 dB rejection of the ground-reflected GPS signals. [29] After several design iterations, antenna systems were constructed consisting of:

- A vertically-polarized dipole-array antenna for reception of satellites with elevation angles between five and 30 deg, and
- A right-hand circularly-polarized high-zenith antenna for reception of satellites with elevation angles above 30 deg.

The dipole-array antenna is designed for both LAAS reception and for pseudolite transmission. The design considerations for the dipole-array antenna are provided in reference [18]. Some of the key features of the dipole-array antenna are:

- Rejection of ground reflections is greater than 35 dB for elevation angles between 5 and 20 deg and greater than 30 dB for elevation angles between 20 and 35 deg;
- Antenna aperture (size) is approximately 2.2 m;
- Antenna gain difference between 5 and 0 deg is greater than -15 dB, which results in a rejection of ground-based interference sources of at least 15 dB;
- Antenna gain at 5 deg is approximately 10 dB better than a standard GPS surveying antenna (circularly-polarized patch antenna on a 1-ft diameter ground plane).

The latter item is very significant. A higher antenna gain results in a stronger GPS signal, which allows the receiver to acquire the GPS signals faster and more reliably at lower elevation angles. A GPS receiver using the dipole-array antenna typically acquires a rising GPS satellite 10 to 20 min earlier than one using a standard GPS antenna.

For the high-zenith antenna, a patch antenna placed in a 2-ft diameter choke-ring was used. Although the ground multipath rejection for the choke-ring antenna is not as good as that for the dipole-array antenna, it was sufficient for a preliminary assessment of antenna system performance. It is also noted that receivers using the choke-ring antenna would rarely track satellites reliably below an elevation angle of 10 deg. Current research is focused on improving the high-zenith antenna.

Two GPS receivers are used for each antenna system. In principle, only two separate front-ends are required, but the use of two separate receivers was a faster way to achieve the system prototype. The hardware delay difference between the two antennas is corrected as follows:

1. Measurements from both the dipole-array antenna and the high-zenith antenna are translated to a common location.
2. Changes in the accumulated Doppler shift averaged over all satellites that are common between the two antennas are used to update the hardware delay in real time.
3. Whenever a satellite is common between the two antennas and its elevation angle is between 25 and 35 deg, then the difference in the pseudorange measurements between the two antennas is used to initialize and adjust the hardware delay.

Note that once an initial value for the hardware delay is found, only the accumulated Doppler shift measurements are required to continuously update the hardware delay for changes in the clock and hardware delay differences between the two receivers.

Smoothing of the pseudoranges with a 100-second time constant takes place after the data from the two GPS receivers is combined. The smoothing filter is implemented using the following two equations.

$$PR_{k+1} = PR_k + \left(AD_{k+1} - AD_k\right)$$

$$PR_{k+1} = PR_{k+1} + \frac{1}{n}\left(PRM_{k+1} - PR_{k+1}\right)$$

Where, *PR* is the smoothed pseudorange, *AD* is the accumulated Doppler shift measurement, *PRM* is the measured pseudorange, and *n* is the number of measurements processed in the filter or $n = 100$ if there are more than 100 measurements processed in the filter for samples taken at a rate of one per second.

Accumulated Doppler shift measurements are continuous to within a few millimeters at the point that the measurements are switched from one antenna to the other at the 30-deg elevation switch-over angle. At that angle, the measured pseudoranges into the filter are switched from one antenna to the other. This ensures a continuous smoothed pseudorange around the switch-over angle between the two antennas.

2.3 Implementation of Integrity Equations

LAAS integrity equations have recently been selected by RTCA Special Committee 159, Working Group 4A. These equations are discussed in detail in [30]. The integrity concept is to compare differential corrections from different ground references. This results in the following test statistics, which are also referred to as B-values:

$$B_{mn} = \frac{PRC_{mn} - \sum_{k=1}^{M} PRC_{kn}}{M - 1}$$

Where *m* indicates the reference number, *n* indicates the satellite number, *PRC* is the pseudorange correction, and *M* is the total number of references. In the case of three references, or $M = 3$, the following relation holds for the standard deviation of the pseudorange corrections and that of the test statistic:

$$\sigma_{PRC} = \sigma_B \sqrt{6} \approx 2.5 \sigma_B$$

Typical B-values for the prototype LAAS are on the order of 3 cm. This corresponds to a standard deviation of the smoothed pseudorange corrections of approximately 7.5 cm. The detection thresholds are set at +0.4 and -0.4 m, which corresponds to the derivation provided in [30] for a pseudorange correction noise of 15 cm. The excellent noise levels for the prototype system support the use of a value smaller than the 15 cm for the pseudorange correction noise. However, the current assumption is that the pseudorange correction noise is bounded by a Gaussian distribution with a standard deviation of 15 cm. Further investigations are required into the actual distribution of the pseudorange correction noise.

2.4 Flight Test Description

The LAAS system as described in the previous sections was flight tested at the FAA William J. Hughes Technical Center at the Atlantic City, International Airport in New Jersey in August of 1997. The Ground Subsystem was fielded at the FAA experimental heliport. Three antenna systems were installed in an equilateral triangle with sides of approximately 100 m. Each antenna was placed at a height of approximately 1.2 m above the ground.

The flight test aircraft, FAA's Boeing 727, carried the LAAS Airborne Subsystem. Both manual and autocoupled approaches were flown to runways 13, 31 and 04. Straight-in approaches were flown with a final approach segment of at least 10 nmi.

Two truth systems were used during the flight test:

1. Ashtech Z-12 L1/L2 GPS receiver with PNAV^{TM} software for post-processing of the data collected during the flight test period. One receiver was located on the ground at a

known location, while the second receiver was on the aircraft connected to the same antenna as the aircraft LAAS subsystem. Accuracies on the order of 0.1 m (1 σ) in each coordinate axis can be obtained by post-processing the data collected from the ground and aircraft receivers for distances of less than 5 km with respect to the ground receiver.

2. Laser tracker, which has angular accuracies of 20 arcsec (1 σ), and a range accuracy equal to 1 ft at a distance of 5 nmi.

During previous tests, it was shown that the above two truth systems agree to within 0.1 m in vertical position determination at distances of less than 1 km. Therefore, all flight test results are shown with respect to post-processed data from the Z-12 truth reference system.

2.5 Flight Test Results

A total of 45 approaches to 3 different runways were analyzed in terms of along-track, cross-track, and vertical sensor accuracies. Figures 2-4 through 2-6 show the LAAS performance with respect to post-processed Z-12 truth reference data. The horizontal axes show the distance in nautical miles with respect to the touch down zone (TDZ), while the vertical axes show the differences between the Z-12 truth reference and the LAAS sensor data. Table 2-1 summarizes LAAS performance at the 100-ft decision height. The 95 percent performance numbers are estimated by the sum of the absolute value of the mean and twice the standard deviation. The Vertical Dilution of Precision (VDOP) during all approaches was generally less than 2, which means that the satellite geometry was good during all approaches.

Table 2-1. LAAS Sensor Accuracy Summary

Coordinate	Mean (μ)	Standard Deviation (σ)	95% $\|\mu\|+2\sigma$
Along-track	0.11 m	0.13 m	0.37 m
Cross-track	0.04 m	0.15 m	0.34 m
Vertical	0.08 m	0.31 m	0.70 m

In Figure 2-6, it is noted that most approaches are clustered closely together, except for four approaches that have vertical errors of up to one meter at the 100-ft decision height. Investigations are underway to determine the cause of these larger errors. Even with these four approaches included in the data analysis, the vertical performance of 0.7 m (95%) is well within the proposed vertical sensor accuracy requirement of 2.0 m (95%) at the 100-ft decision height [26].

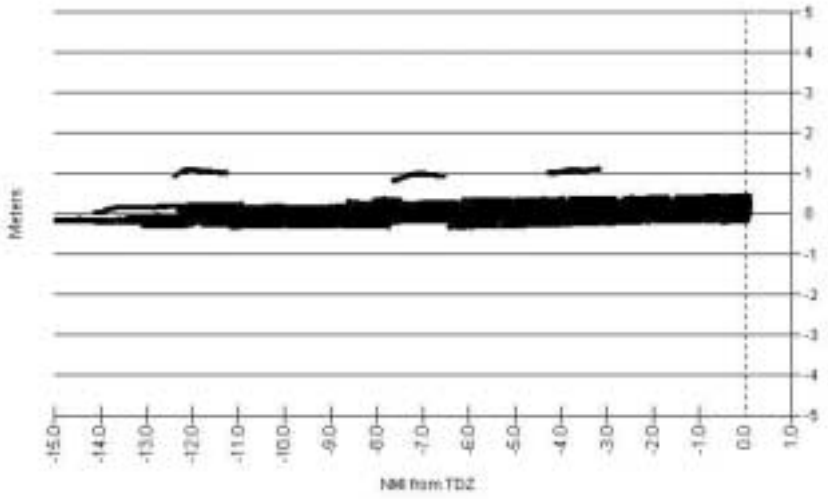

Figure 2-4. LAAS Along-Track Sensor Accuracy

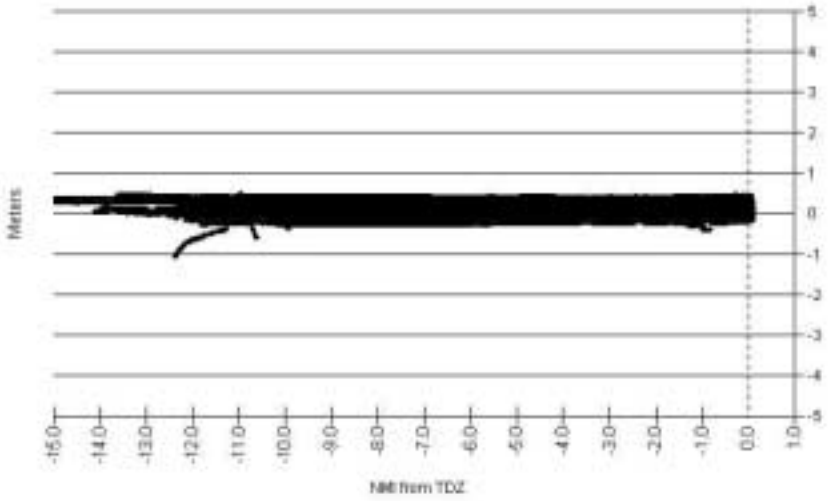

Figure 2-5. LAAS Cross-Track Sensor Accuracy

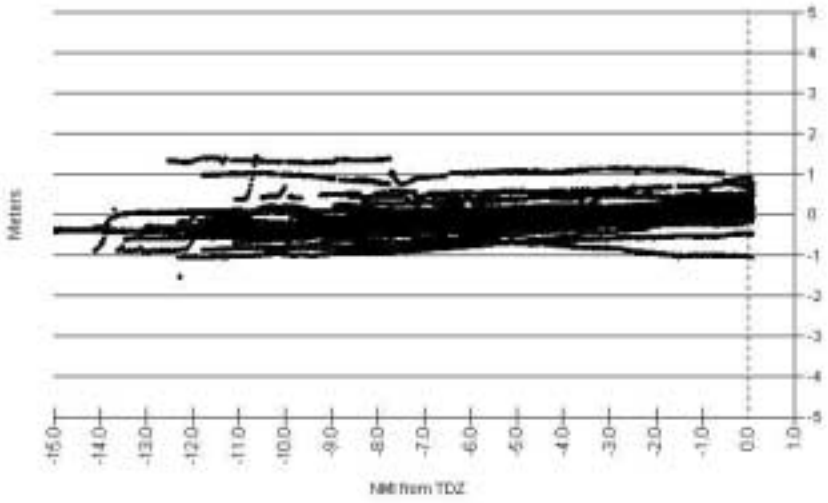

Figure 2-6. LAAS Vertical Sensor Accuracy

3.0 GPS INTEGRATED WITH AN INERTIAL MEASUREMENT UNIT

Low-cost Inertial Navigation System (INS) sensor technology has evolved rapidly over the last decade with the development of less-expensive and higher-accuracy inertial measurement units (IMU). Developments in the field of the Global Positioning System (GPS) have also matured over the past decade to provide reliable centimeter-level accuracy in a relative sense for stand-alone GPS, and in an absolute sense for differential GPS (DGPS).

Table 3-1. Inertial and GPS/Inertial Aviation Applications

DESCRIPTION	ACCURACY	DURATION	APPLICATION
Attitude & Heading Reference System	0.1 - 1 deg	2 minutes	Artificial Horizon Advanced (Perspective) Displays (need pos & vel)
Aid GPS Code Tracking Loops	0.1 m/s for 1-s aiding	0.5 - 10 s	Improve tracking margin up to 30 dB Non-differential: 20-m accuracy Differential: 5-m accuracy
Aid GPS Carrier Tracking Loops	< 5 cm	0.5 - 10 s	Improve tracking margin up to 30 dB Differential: sub-meter accuracy (Precision Approach)
Positioning: Coast after loss of GPS	< 500 m	seconds - minutes	Continuity for Non-Precision Approach
	sub-meter	seconds - minutes	Continuity for Precision Approach and Aircraft Surface Movement Guidance and Control
	meter-level	10 minutes	Complete Precision Approach
	meter-level	30 minutes	Complete Taxiing
Positioning: INS stand-alone	< 500 m	several hours	Non-Precision Approach & Terminal Navigation - entire flight
	km-level	several hours	Enroute Domestic and Oceanic - entire flight

Table 3-1 lists aviation applications of both inertial and integrated GPS/inertial systems, along with approximate accuracy requirements and the period of time over which the accuracy must be achieved. It is noted that at the time of this writing, no clear operational requirements for most of the applications listed in Table 3-1 exist.

The least demanding application for a strapdown IMU is its use in an artificial horizon. This application is expected to increase with the introduction of advanced displays for General Aviation. Next, two applications are listed for aiding of GPS code and carrier tracking loops. Both are intended to improve the receiver tracking margin by up to 30 dB with respect to an unaided receiver. To aid the code tracking loop over a period of time of

1 s, a velocity reference is required with an accuracy of 0.1 m/s. For a DGPS application, the positioning accuracy would be on the order of 5 m, due to code tracking noise. If better accuracies are required, then the carrier tracking loop must be aided, which requires an accuracy of approximately 1/4 wavelength or 5 cm for the GPS L1 frequency at 1575.42 MHz. An improved tracking margin provides for robust tracking of GPS signals in the presence of interference.

If the GPS signals are no longer available due to excessive interference, signal blockage, or satellite outages, then the coasting performance becomes important. For these applications, it is assumed that the inertial sensors are calibrated before loss of GPS. Temporary loss of GPS would need to be filled-in with inertial guidance to maintain continuity. If the operational procedure, such as a precision approach, is to be completed, then meter-level accuracy would be needed with a high level of integrity. For example, a Category I precision approach would require that the vertical position error would not be worse than 10 m at the 200-ft decision height above the ground. The last two rows of Table 3-1 list INS stand-alone applications. One example is the current use of triple redundant INS as a primary means for oceanic navigation.

The focus of this investigation is to determine the feasibility of 1) Centimeter-level calibrated IMU performance for GPS code/carrier tracking loop aiding to improve the GPS tracking margin; and 2) Coasting during precision approach and surface movement guidance and control applications to mitigate loss of continuity.

For both cases, a low-cost IMU will be calibrated with centimeter-level DGPS (also referred to as kinematic GPS). It is noted that increased tracking and continuity performance can also be obtained with stand-alone GPS, since the GPS relative accuracy is on the order of centimeters.

Coasting performance will be evaluated for two DGPS outage scenarios:

1. A DGPS outage during straight-and-level motion; and,
2. A DGPS outage just prior to the initiation of a horizontal-turn maneuver.

3.1 Observability and Error Sources

Short-term, cm-level inertial performance is quite different from navigation-type performance. Since the error sources of low-cost instruments are not constant over time, it is not possible to observe all error sources. For example, the difference between a mis-orientation error and an accelerometer bias error cannot be observed. A small tilt error of 0.1 degree would result in a bias in the horizontal plane of $\sin(0.1^o)g = 1.7$ cm/s^2. This bias error results in a position error in the measurement direction of the accelerometer of $(0.017)/2*t^2$. After 1 s, the position error is 0.0085 m, while after 10 s, the error is 0.85 m. This type of error would be similar to a typical low-cost accelerometer bias error of 1 cm/s^2. In the short-term, it would not be possible to distinguish between a mis-orientation and an accelerometer bias error, unless special, high-dynamic maneuvers are performed.

Another important error source is accelerometer noise. For example, double integration of accelerometer noise with a standard deviation of 1 cm/s^2 at a rate of 100 samples per second, results in position noise in the measurement direction of the accelerometer of 0.0006 m after 1s; 0.018 m after 10 s; and 0.577 m after 100 s.

3.2 Hardware Design

Figure 3-1 shows a high-level block diagram of the system designed for the purpose of DGPS-INS integration. The reference facility consists of a GPS receiver and GPS antenna accessories. The reference antenna is kept at a known, surveyed location (surveyed in the WGS-84 coordinate system). The GPS measurements include pseudoranges, carrier phases and satellite orbital parameters. For real-time implementation of the system, GPS data are continuously sent over a data broadcast system to the airborne unit. A data broadcast system is not included in the system used for the purpose of this research. Instead, all data are collected for off-line analyses.

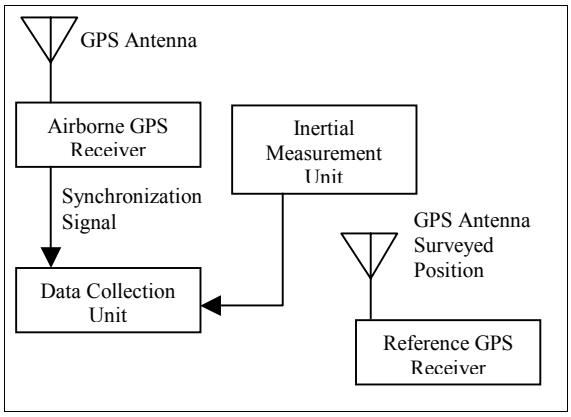

Figure 3-1. Hardware Implementation

Due to aircraft dynamics, the accuracy of the integration of IMU and DGPS data is not only affected by the time at which the measurements occur but also is dependent on the relative location of the GPS antenna and the IMU. For this reason, a tight hardware coupling (data collection synchronized to the GPS timing pulse) is designed for data collection to avoid data extrapolation. Furthermore, both sensors are placed physically close to one another in order to minimize lever-arm effects. The IMU selected for the integration is the Systron Donner Motion Pack™. Key features of the Motion Pack™ IMU are:

I. Analog outputs; this property allows the implementation of an interface that synchronizes the IMU measurements with GPS time;
II. Compact, rugged package; enables an aircraft installation where the IMU can be located close to the GPS antenna;
III. Fast startup;
IV. Wide bandwidth (70 Hz for the gyros and 900 Hz for the accelerometers);
V. Reasonable accelerometer noise performance of 1 mg (RMS);
VI. Over 10,000 hours of Mean Time Between Failure (MTBF).

A picture of the Systron Donner Motion Pack™ is shown in Figure 3-2.

Figure 3-2. Motion Pack™ Inertial Measurement Unit

The Motion Pack™ IMU unit outputs analog measurements of three linear accelerations, three angular-rates and temperature. A Digital Signal Processing (DSP) processor with eight-channel simultaneous sample-and-hold (SSH) and 16-bit analog-to-digital (A/D) converter was selected for the data collection and processing. Due to the simultaneous sample-and-hold capability of the A/D converter, the samples collected from the A/D conversion are obtained at the same instant in time. The selected converter card also has a Direct Memory Access (DMA) data transfer capability, an external trigger for data collection timing purposes and internal clock generation capabilities for implementing advanced timing applications.

The GPS receivers chosen for the purpose of the research are dual-frequency Ashtech Z-XII. The Z-XII one pulse-per-second timing output pulse is used to trigger the IMU measurements.

3.3 Navigation and Error Equations

At any instant, the user position, velocity and attitude are computed by using the raw accelerometer and gyro measurements along with the knowledge of initial position, velocity, and attitude. Attitude initialization is performed using techniques summarized in [12]. The process of the position, velocity, and attitude update occurs in two separate phases. First, the gyro measurements are used to update the body attitude. Next, the orientation information from the attitude-update routine is used along with the accelerometer measurements to update position and velocity. Earth-rate and transport-rate compensation are applied to correct for the rotation of the earth and the rotation of the locally-leveled platform with respect to the earth due to its horizontal velocity with respect to the local origin.

The integration of GPS and INS is often used to capitalize on the synergistic benefits of both systems, the long-term stability of GPS and the short-term robustness of the INS. The process of integration is achieved by evaluating the error coefficients that model the IMU correctly during the availability of valid DGPS positions. During a DGPS position outage, the estimated IMU error coefficients are utilized to enhance accuracy in standalone IMU positioning.

A closed-loop version of the Kalman-filter is usually implemented for the purpose of integration. This configuration is used due to the fact that the other (open-loop) configuration may lead to overflow problems in the computer's numerical computations. However, an open-loop implementation of the Kalman-filter provides better insight into sensor error behavior. For the purpose of this research, an open-loop configuration is implemented to investigate the variation of error coefficients.

In a GPS/INS integration, the Kalman filter typically estimates a minimum of 15 state-variables:

I. 3 position error coordinates
II. 3 velocity error coordinates
III. 3 attitude errors
IV. 3 accelerometer bias errors
V. 3 gyro drift errors

Biases on both accelerometers and the gyros were modeled as constants, due to the limited observability of these state-variables.

Figure 3-3 shows the physical placement of the Systron Donner IMU with respect to the GPS antenna.

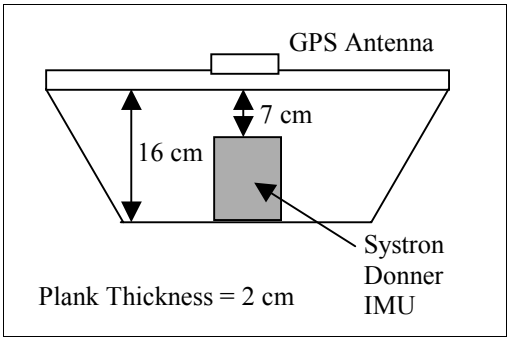

Figure 3-3. Relative Placement of the GPS Antenna and the IMU

Both van and flight test configurations were similar to the one indicated in Figure 3-3. Separation between the IMU and the GPS antenna phase center was carefully measured and used in the navigation equations to reduce lever-arm errors.

3.4 Van and Flight Test Results

The Kalman filter innovations were evaluated for both the van and flight tests. These innovations are the difference between the propagated IMU position and the DGPS position solution, which is accurate to within a few cm. It was observed that the innovations are on the order of 1 cm for one-second update intervals, which corresponds to the rate at which DGPS positions are available. Details regarding the innovations can be found in [12]. This result indicates that it is feasible to perform carrier tracking loop aiding for periods of time up to 1 s.

To evaluate coasting accuracy for longer time periods, several DGPS-signal-outage scenarios were simulated in the software to evaluate the performance of the calibrated low-cost inertial measurement unit under different van and flight dynamics.

Table 3-2 summarizes the coasting performance for both the van and flight tests.

Table 3-2. IMU Error Growth

Scenario	RSS ERROR AFTER COASTING	
	5 s coasting	10 s coasting
Van Test	1.3 m	6 m
Flight Test: Level	8 m	22 m
Flight Test: Turn	30 m	160 m

From the results presented in this section, it is concluded that GPS carrier tracking loop aiding is feasible for integration time periods up to 1 s. Sub-meter coasting intervals for surface applications could be on the order of several seconds. For flight applications, coasting intervals can be up to 1-2 s for low dynamics, but cannot exceed 1 s during turns.

To improve the observed coasting performance, either better inertial sensors should be used, or innovative processing techniques could be used that maximize short-term integrated GPS/IMU performance, as proposed in [31].

4.0 ON-AIRPORT RANGING PSEUDOLITE

The concept of ground based GPS-like transmissions, now called pseudolites, has been around ever since the early development of the GPS (i.e., 1977 Yuma, AZ test). [32] Research over the past seven years has concentrated on the addition of an APL to increase the availability of a LAAS. It has been demonstrated that a code based system, with code and carrier measurements being passed on a VHF data link [2], can provide the accuracy, continuity, and integrity for a CAT III system. In order to realize an increase in availability with the addition of an APL(s) to a LAAS, the APL must be of high quality and able to be used as a ranging source. Integration of the APL into the DGPS solution must not induce the error sources to exceed that for the precision approach system supported. The primary goal is the addition of a ground-based APL such that it improves the DGPS LAAS availability.

4.1 Isolating Major APL Error Sources

Two of the major error sources for APLs in precision approach are ground multipath and the large power level variation over the final approach path. To assess these major error sources, a prototype APL subsystem was developed such that it could operate at any frequency in the L1 band (L1 $\pm$ 10 MHz), at any code rate, and in a one or two receiver configuration mode; a second APL only receiver is added if the APL operating frequency is outside the passband of the GPS receiver. (In a single receiver configuration both the GPS and APL signals are received with the same receiver.)

The large power level variations that an APL subsystem has to deal with affects the APL signal structure such that EMI is not induced on the nominal DGPS performance of the LAAS. When the APL frequency of operation is within the passband of the GPS receiver, several modifications must be made to the APL signal structure. To isolate the effects from error sources induced by ground multipath and error sources induced by the APL signal structure, an APL with a frequency offset of L1 + 8*(1.023 MHz) = 1583.6 MHz was tested. Use of this prototype was extremely useful in terms of assessing APL subsystem performance, error components, system parameter trade-offs, and their sensitivity to design parameters. The MLA was designed with APL requirements included and then tested with this APL configuration to assess its effectiveness to limit ground multipath for APL applications in precision approach [4]. One of the major shortfalls of the L1 + 8 MHz configuration was that the dual receiver configuration tested had a random clock start up bias of $\pm$ 49 nsec. This random bias was $\pm$ 1 clock cycle of the internal 20.473 MHz clock even though both receivers were tied together with a common rubidium frequency standard and GPS time was transferred to the APL receiver for pseudorange calculations. The need to eliminate this clock bias error is the major reason why a single GPS and APL receiver configuration was used for the majority of testing.

4.2 APL Transmitter

The APL transmitter consists primarily of a GPS signal generator with power amplifiers and pulser circuit. This APL transmitter is shown in Figure 4-1. The APL signal generation is performed with a modified Northern Telecommunications (NORTEL) GPS Simulator with a common 10.23 MHz oven controlled crystal oscillator (OCXO) frequency reference. Pseudorandom noise (PRN) code 34, in compliance with reference [5], is used with an arbitrary GPS Week number of 800. A power level of -37 dBm is generated directly, followed by a stage of amplification. Pulsing is then accomplished with two high-isolation high-speed RF switches. The isolation of the RF switches was measured to be 118 dB of on/off isolation "on the cable". A final stage of power amplification follows for a final peak power of +12 dBm. The RF amplifier and pulser RF network is enclosed within a RF shielded enclosure so that a truly pulsed APL signal is seen at the LAAS receivers. The pulser control line into the RF shielded enclosure was controlled from the LAAS Ground Station (GS) location via a 100-meter cable. The pulse on/off timing was driven from GPS 1 pulse per second (PPS) at the LAAS GS GPS and APL receiver. The pulsing format was 310 C/A chips on and 806 C/A chips off at a 1/11 th code cycle rate, thus sliding the APL transmission through each epoch of the receivers integration window. The transmitted duty cycle was 27.8 %. The pulsing format chosen was primarily driven from the requirement to operate in a linear operation region (non-saturating) of the receiver. The APL equipment is housed in a ruggedized enclosure and located in close proximity to the transmitting MLA.

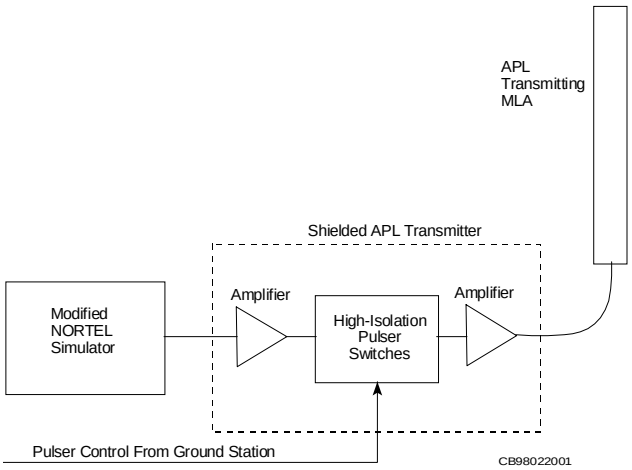

Figure 4-1. On-L1 C/A Prototype APL Transmitter Block Diagram

4.3 APL Multipath-Limiting Transmitting Antenna

To minimize ground multipath a MLA is used for APL transmission. This antenna is similar to that used in other land based transmitting navigation systems such as DME where the elevation pattern rolls off sharply to minimize ground reflections. Figure 4-2 is a plot of the elevation radiation characteristics at L1. Figure 4-3 is a photograph of the APL transmitting MLA. This MLA has an omni-directional radiation characteristic in

azimuth. The gain at higher elevation angles provides for aircraft "fly-by" coverage. This pattern provides for a high desired-to-undesired (D/U) ratio.

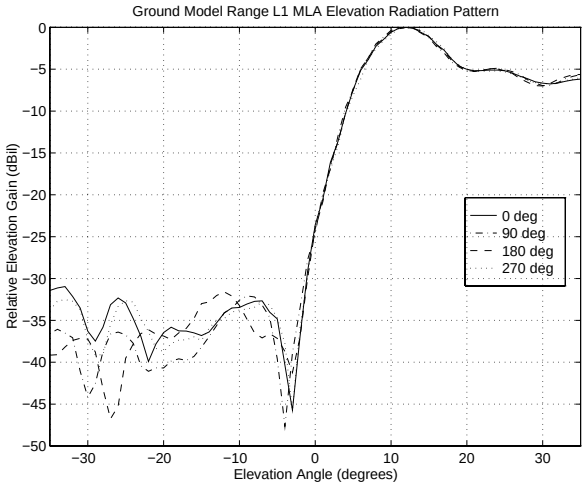

Figure 4-2. MLA Elevation Radiation Plot for S/N003, where 0 dB Equals Approximately 7.5 dBil

Figure 4-3. MLA used for APL Transmission

4.4 APL Receiving Subsystem in the Prototype LAAS

APL Receiving Subsystem at the Ground Station: The distance between the APL transmitting antenna and GS reception antenna was chosen to be approximately 80 meters based on the height of each antenna and the first null (at 3^o down) in the elevation pattern of the MLA to minimize ground multipath. Due to siting and logistic constraints at the Ohio University (OU) UNI Airport, the LAAS GS was placed approximately 1000 feet prior to the runway threshold in line with Runway 25.

A two-GS configuration for prototype APL signal reception used in developmental tests. The APL subsystem was integrated into the OU/FAA LAAS described in [9]. The APL signal can be received by either the high-zenith antenna (HZA) used for high elevation GPS satellite vehicle (SV) reception or MLA (for low elevation GPS SV reception).

One hundred meters of low-loss heli-axial cable connected the field antennas to the LAAS GS located in a mobile van. Data has indicated that satisfactory APL performance can be gained with either APL reception on the top HZA or the lower MLA based on antenna siting constraints. With good antenna siting APL reception with the MLA is preferred. With poor antenna siting (as the case at the Ohio University UNI Airport) the HZA is preferred; a passive antenna with choke ring was used. For the GPS Blanking Box ("desired GPS only path") a single TTL switch is in series to "blank" the APL signal during the time when it is present.

The timing control for all blanking is via a GPS 1 PPS input and micro-controller. In the ground station a guard time of approximately 2 μ seconds is added to ensure complete blanking overlap. For this desired GPS only path the level of blanking was not complete but only to a comparable level as is done on the desired GPS and APL signal path. The APL power level was turned down/blanked by approximately 35 dB and not totally turned off. This was done to assure the carrier-to-noise (C/N_o) calculations in the receivers were comparable. Within the APL manual gain control (MGC) and GPS Blanking Box, the GPS and APL composite signal was split into a desired GPS sub-path and desired APL sub-path with a power splitter. In the desired GPS signal sub-path the APL signal was blanked "totally" with two series combination TTL switches; the two TTL switches provided an on/off isolation of approximately 70 dB. In the APL sub-path a programmable attenuator was used to manually control the gain of the APL signal presented to the receiver. The APL signal was usually turned down by about 25 dB. Since the APL signal was pulsed and the APL blanking occurred in the other sub-path (desired GPS sub-path), the attenuator operated in a continuous time fashion (i.e., did not pulse). The power level controlled APL signal in the desired APL sub-path (with the GPS signals now below it by about 25 dB), and the desired GPS blanked signal in the desired GPS sub-path (APL signal at about the same level as GPS) were then recombined. To minimize signal fading, both paths were calibrated with a network analyzer. All cable lengths were minimized to preclude temperature variation effects.

All GPS and APL receivers were NovAtel 3951R Receivers with standard or modified boot files for APL reception. A rubidium frequency standard was used to tie

measurements from the HZA and MLA antennas so the phase variation as function of GPS SV elevation angle could be observed; the rubidium standard would not be required for an operational system. The VHF Data Link (VDL) used a horizontally polarized 8-ary differentially phase shift keyed modulation formatted signal to support DGPS operation. [9]

APL Receiving Subsystem at the Aircraft: All signal reception is with a single top-mounted right hand circularly polarized (RHCP) passive L1, L2 patch antenna. Flight data presented here was collected with the Ohio University DC-3 Aircraft. The antenna location is top-mounted on-centerline at flight station 143.0. The RF signal was split and fed into an Ashtech Z-12, used for truth, an unmodified NovAtel 3951R GPS Only Receiver used for APL interference assessment and DGPS reference, and the combined GPS and APL NovAtel Receiver via the APL AGC and GPS Blanker Box.

For APL applications a wide dynamic range is required due to free space $(\lambda/4\pi R)^2$ losses. The variation in power from a minimum operation range of 80 meters to 10 nmi at L1 is 47.3 dB, not including antenna pattern and other variations. Thus, the dynamic range required for an APL channel far exceeds the dynamic range available in a GPS receiver.

Early laboratory and flight tests revealed an un-calibratable error source that was present as the receiver saturated over a 63 dB dynamic range. Due to these nonlinear effects in the receiver, an AGC approach was taken. This approach was done at RF so that the RF power level was controlled and the receiver never saturated.

The APL AGC and GPS Blanker Box, prior to the GPS and APL receiver is similar to the ground circuit. Again GPS 1PPS timing was used from the GPS and APL receiver for blanking control. Again the GPS and APL signal was split into a desired GPS sub-path and desired APL sub-path with a power splitter. In the desired GPS sub-path the APL signal was blanked "totally" with two series combination high-isolation switches; each switch provided an on/off isolation of 63 dB and the total on/off isolation was measured to be 118 dB. A guard time of 62 C/A chips was used to support a guard time of approximately 10.0 nmi. The airborne blanking sequence was 372 chips on and 744 chips off at a 1/11 code cycle rate, again sliding through each epoch integrated in the receiver. This could produce a maximum loss in GPS C/N_o of about 2 dB, which was not a problem with our low-noise/high gain pre-amplifier configuration. In the APL sub-path a programmable attenuator was used to automatically control the gain of the APL signal presented to the receiver. This programmable attenuator was driven by the APL (PRN 34) C/N_o measurement and maintained between 42-43 dB/Hz. Since the APL signal was pulsed and the APL blanking occurred in the other sub-path (desired GPS sub-path), the attenuator operated in a continuous time fashion (i.e., did not pulse). This RF AGC controlled the power level of the desired APL signal (with GPS below it) and the desired GPS Blanked (APL signal blanked "totally") were then recombined. To minimize signal fading, both paths were calibrated with a network analyzer. All cable lengths were minimized to preclude temperature variation effects.

For an on-L1 APL, pulsing (with high total on/off isolation) is required to mitigate EMI. Laboratory tests indicate that the amount of EMI protection is directly proportional to the duty cycle. [33] Laboratory tests indicate that the C/N_o calculations for the receivers tested were inaccurate for pulsed APL signals. The C/N_o calculation became more non-linear as the duty cycle decreased. Hence, at low duty cycles the linear operating region ("comfort zone") became extremely small. Since the desired operation region was a linear portion of C/N_o indication in a non-saturation region, the duty cycle had to be high enough so that successful C/N_o tracking could occur to drive the RF AGC. These were the primary factors to operate the APL at a duty cycle of 27.8 %. With C/N_o calculations for pulsed signals, lower duty cycles are likely supported in a linear region of operation within the GPS/APL receiver.

4.5 Prototype On-L1 C/A APL in LAAS Calculations

Code and carrier measurements were taken from the system NovAtel receivers and brought to the navigation processor. Code smoothing by the carrier, within the receiver was moderate at a time constant of approximately 10 seconds. Since the APL 50 bps message or chip edges at generation were not synchronous with GPS timing, the APL pseudorange measurements were first moduloed down by a C/A epoch at each receiver. This is a valid operation since the operating range from the time of transmission to the time of reception is less than a C/A epoch (299,792 meters). Next, the APL pseudorange measurements were smoothed by the carrier consistent with the LAAS [9] smoothing, using the following equations:

$$PR_p(k) = PR_s(k-1) - [\phi_m(k) - \phi_m(k-1)]\,\lambda$$
$$PR_d(k) = PR_m(k) - PR_p(k)$$
$$PR_s(k) = PR_p(k) + \alpha(k)\,[PR_d(k)]$$

where:

PR_p = Pseudorange Measurement Propagation Term,
ϕ_m = Accumulated Doppler Measurement,
λ = Carrier Wavelength in meters,
PR_m = Pseudorange Measurement,
PR_d = Difference Between PR_m and PR_s points,
$\alpha(k) = 1/\tau$ = filter constant,
τ = smooth time constant, $1 < \tau < 100$ seconds,
$PR_s(k)$ = Smoothed Pseudorange Measurement.

APL integration into the LAAS can be analyzed with respect to the pseudorange or position domain standpoint. For pseudorange domain analysis an APL single difference (SD) was taken between the ground receiver (subscript 1) and user receiver (subscript 2) in a similar fashion as is done for DGPS. [34] This removes all common errors in the APL signal generation (arbitrary message, APL transmitter frequency reference drift, etc.,). The calculation is as follows for i = 1 to 34:

$$SD^{i}_{PR,2\text{-}1} = PR^{i}_{2} - PR^{i}_{1} + \Delta\tau_{2-1}$$

The APL double difference (DD) is taken in a similar way between the APL SD and a GPS SD to remove the GPS/APL receiver clock bias term ($\Delta\tau_{2-1}$) as described by:

$$DD^{ij}_{PR,2\text{-}1} = (PR^{i}_{2} - PR^{i}_{1}) - (PR^{j}_{2} - PR^{j}_{1})$$

DGPS and differential APL (DAPL) position integration is accomplished in a least-squared sense. Position analysis will be with respect to an East, North, Up (ENU) coordinate system. Differential corrections using one and two GS APL receivers were tested. The 'bias" B-values, consistent with LAAS integrity methodology described in [8], are used as a test statistic to indicate the similarity between the pseudorange correction formed from each GS site, after transformation to a common point. B-values are similarly calculated for the APL using the following:

$$B^{n}_{m} = \frac{PRc^{n}_{m} - \sum_{k=1}^{M} PRc^{n}_{k}}{M - 1}$$

where:

PRc = Pseudorange correction,
M = Number of GS sites,
m = Reference Receiver Number,
n = SVID or APL PRN Number.

4.6 Prototype On-L1 C/A APL in LAAS Performance

The location of the APL transmission antenna, and the GS reception antennas were surveyed with an Ashtech Z-12 Receiver. The current peak transmitted power is +12 dBm, which is limited primarily by the components in the current APL RF transmitter. This power level supports an APL operation range of approximately 6-8 nmi and could be increased to support increased operation ranges with consideration to EMI. At this power level and duty cycle, EMI was not recorded by an Ashtech Z-12 GPS Receiver located atop the OU Hanger 578 meters from the APL transmitter. Additionally, using the standard NovAtel 3951R GPS Receiver and a Trimble LTN-2000 GPS Receiver aboard the aircraft, EMI was not observed from the APL transmission during a typical approach path. It should be noted however that EMI was observed in the GS receivers if they were not blanked. In the absence of blanking, the pulsed APL signal level would be approximately 25 dB stronger than the GPS signal levels. This causes the receiver to loose lock on the weaker GPS SV signals. An operational APL augmentation would use lower pulsing duty cycles which would mitigate this EMI effect. Furthermore, the proposed wideband APL signal structure [35] would render this EMI effect insignificant.

To monitor and detect anomalies in the pseudorange measurements at the LAAS ground station, the B-values are computed between the two ground reference sites. Figure 4-4 shows the B-values for the APL and SVID 19 used in the APL DD calculation for the

HZA. The ground multipath can be observed in real-time from these B-value calculations. For the GS APL DD error analysis the measured APL DD is formed and subtracted from the truth APL DD. This true APL DD is formed using surveyed antenna positions and the SVID 19 orbit data. SVID 19 was used in the APL DD because it had the lowest B-value and hence presumed to be of the best quality. Data indicates that the criteria for the GPS DD should be based on B-value and not simply SV elevation angle. With better antenna siting the APL could be received by the GS MLA antennas and benefit from these MLAs further. Figure 4-5 shows the computed APL DD error. The large spikes in the APL DD are caused when the APL receiver loses lock and the code filter is reset. This loss of lock results when the DC-3 over flies directly between the APL transmitting antenna and APL reception antenna. In this data analysis no PR limit checks were performed (i.e., APL exclusion) but is incorporated in the real-time system. With better antenna siting these events would likely not occur. While this data does still contain some ground multipath, the multipath from the GPS SV used in the single difference is mixed in. The APL transmitting MLA limits the APL multipath and no substantial long-term bias exists.

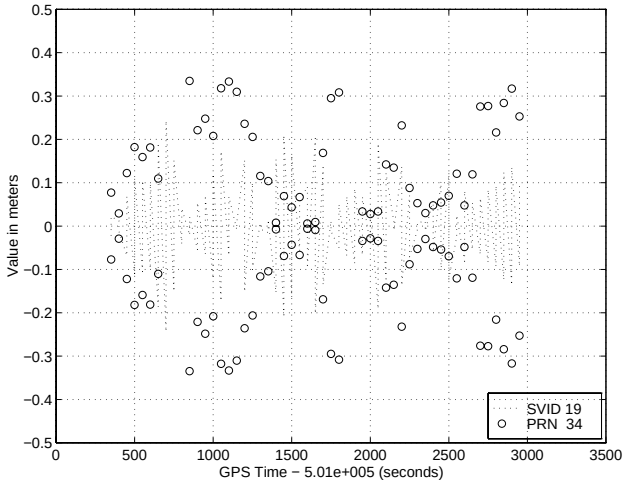

Figure 4-4. B-values for APL DD Calculation at LAAS GS

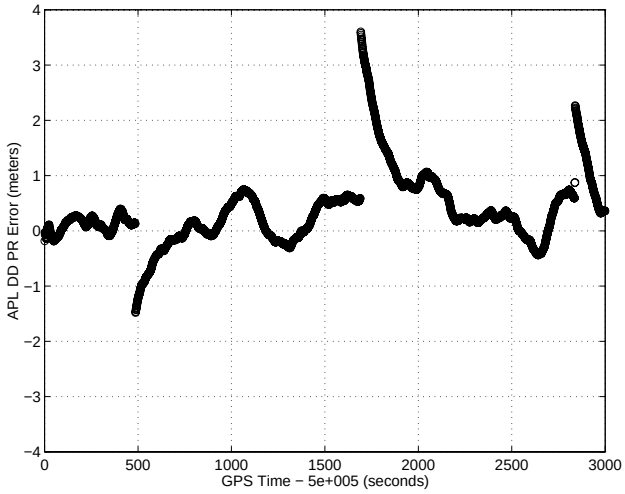

Figure 4-5. Ground APL DD Error Between APL SD - GPS SD and True Range GPS SD Using SVID 19 on 20 February 1998

GPS and APL PR corrections were broadcast in real-time via the VDL, received by the Airborne Processor, and applied to the airborne GPS and APL PR measurements. The DAPL measurements were then incorporated into the DGPS position solution in real-time. The APL was excluded from the position solution if the DAPL PR measurement exceeded a 5-meter spheroid around the DGPS position solution, the APL signal was lost, or invalid ground data was received.

At the beginning of a typical approach, acquisition was fairly rapid where the APL channel was assigned to search over a window of $\pm$ 700 Hz. This window is large enough to cover any temperature variation of the APL frequency reference OCXO and Doppler. Pulsing at the 27.8 % duty cycle, acquisition typically occurred at a C/N_o of approximately 35 dB/Hz. The C/N_o was allowed to increase to a point of 43 dB/Hz where the RF AGC then took control to maintain the C/N_o between 42 to 43 dB/Hz until its dynamic range of 63 dB was expended. At +12 dBm peak transmitted power, power control over a 55 dB dynamic range was performed. Since all approaches were of short range and of low altitude, troposphere corrections were not applied. Not modeling this effect does produce a small amount of error at the maximum range of the APL (6-8 nmi out) but is insignificant by the time decision height is reached. Further investigation into the troposphere errors at these low elevation angle/low heights for APL applications will likely be needed.

Figure 4-6 illustrates a ground track of a typical DC-3 flight approach and shows when the APL was in or out of the DGPS solution. In general, the APL was included in the DGPS/DAPL position solution most of the time, except for period outside the antenna patterns or dynamic range of the APL link.

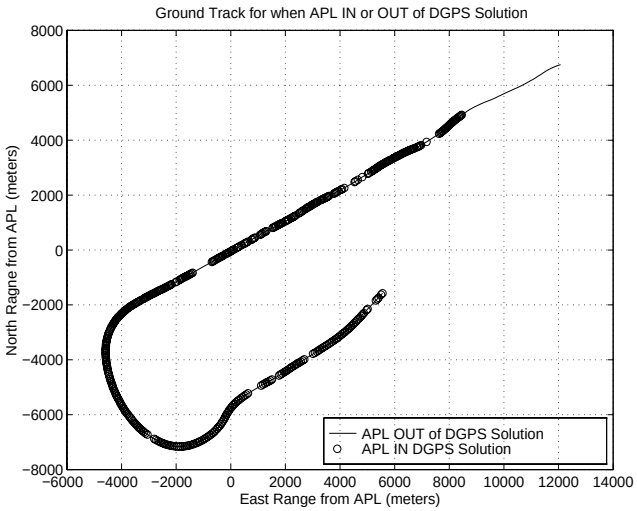

Figure 4-6. Ground Track Illustrating When APL was In or Out of DGPS Solution

The vertical dilution of precision (VDOP) for a typical DC-3 approach loop is illustrated in Figure 4-7. This VDOP is related to the satellite geometry illustrated in the sky plot in Figure 4-8. The beginning of this approach corresponds approximately to the beginning of the sky plot traces where the GPS SVID number is located to the right of the beginning for the respective trace. This good SV geometry corresponds to a good VDOP even without the APL. The benefit of the APL can be seen in Figure 4-7 for the GPS and APL receiver when the APL is incorporated into the DGPS/DAPL solution. The benefit of the APL in VDOP reduction is clearly illustrated. Data has also indicated that when SV geometry is not as favorable then the VDOP reduction can be more dramatic. The VDOP reduction track is not "flat" due to the siting of the APL at the Ohio University UNI Airport prior to the runway threshold where a constant 3^{o} approach path is not maintained.

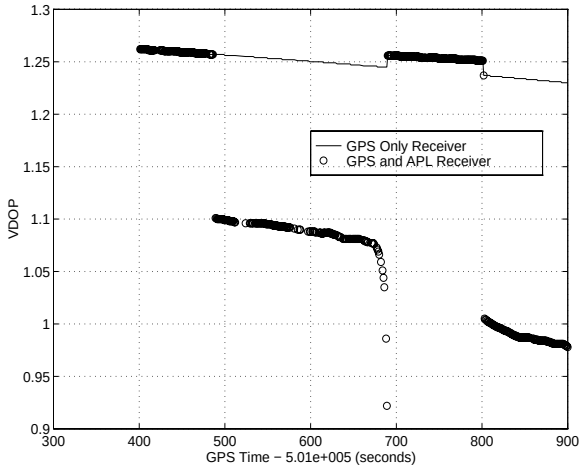

Figure 4-7. VDOP of Typical Approach Loop With and Without APL in Solution

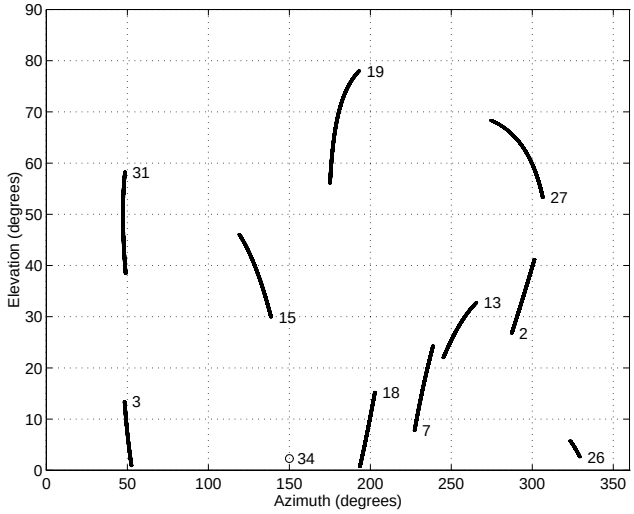

Figure 4-8. Sky Plot of SVID and APL at Ground Station from 501300 < GPS Time < 504000 on 20 February 1998

Figure 4-9 shows typical DGPS/DAPL solution errors over the final phase of an approach. These errors in ENU coordinates are the DGPS solution error without the APL subtracted from the DGPS/DAPL solution error with the APL (The absolute DGPS error with respect to the post-processed kinematic Ashtech Z-12 solution was sub-meter in each ENU coordinate).

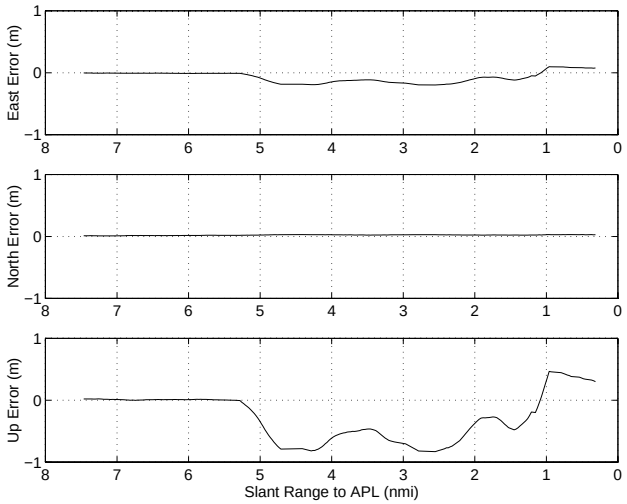

Figure 4-9. Typical Difference Between the GPS Only DGPS Position Errors and GPS/APL DGPS/DAPL Position Errors

In conclusion, a prototype APL has been successfully integrated in a real-time manner into the OU/FAA LAAS. APL signal gain control and blanking has been incorporated to maximize APL tracking performance, while minimizing EMI to nominal GPS performance. Field tests indicate that ground level multipath can be limited using the C/A code and antenna siting to provide a near-zero bias ground reference measurements

suitable for DAPL operation. The prototype system currently supports an operation range of about 6 - 8 nmi with accuracy applicable to precision approach. Real-time DGPS/DAPL position integration without accuracy degradation beyond precision approach limits has increased the availability of the prototype LAAS.

Further research is recommended in the areas of APL signal structure and broadcast antennas to increase the ranging accuracy and to simplify the siting of the APL broadcast antenna.

5.0 FAULT DETECTION AND EXCLUSION

A baseline Fault Detection and Exclusion (FDE) algorithm is developed to: 1) Provide an example of an FDE algorithm; 2) Facilitate the evaluation of different augmented Global Positioning System (GPS) navigation system architectures; 3) Support the FDE test and certification procedures; 4) Avoid having to develop different algorithms for each GPS augmentation; 5) Accommodate flight planning; and 6) Predict the impact of system outages on the Air Traffic Control system.

Rather than performing fault detection, isolation, and reconfiguration (FDIR), the baseline algorithm attempts to find a set of redundant measurements that does not cause a detection. Isolation of the malfunctioning signal is not required. For example, if satellite 3 malfunctions and causes the FDE algorithm to detect an inconsistency, then a different set of redundant measurements must be selected such that the detection does not occur. Although unlikely, this new set could still include satellite 3. No action is necessary if satellite 3 was not part of the navigation solution, or if the detection did not occur.

The baseline FDE algorithm is based on the parity space concept. The parity space concept used here is identical to well-known FDI techniques for redundant inertial navigation systems, see [36 - 39]. The parity space concept was first applied to GPS in [40]. The inputs to the parity space algorithm are the maximum allowed probabilities of false detection and of missed detection, the measurement noise standard deviations, and measurement geometry. The output of the algorithm is the detection threshold and the Horizontal Integrity Limit (HIL), which defines the smallest horizontal radial position error that can be detected with the required probabilities of false and missed detections. This particular algorithm was selected, because it has the following required characteristics:

- A procedure for setting thresholds and determining algorithm performance without having to rely on extensive simulations,
- Accommodation of unequal RMS error levels among measurements, with usage of covariances as well as geometry,
- Sufficient completeness and analytical rigor to allow formulation and substantiation of confidence levels attached to all key parameters (missed detections, algorithm unavailability),

5.1 Algorithm Requirements

GPS augmented position integrity performance requirements are provided in Table 5-1. For example, during the Terminal phase of flight, the algorithm must detect with probability 0.999 when the horizontal radial position error is larger then the 1.0 nmi alert limit. This detection must occur within a period of time of 10 seconds after the position error exceeds the alert limit.

The baseline algorithm is designed to provide a minimum, high level of availability, although it is possible to achieve an even higher level of availability. For example, one could design an all-in-view algorithm rather than the best of n+2, where n is the number of

unknowns (such as three position coordinates and time) to be solved for. Given the baseline algorithm and the particular GPS augmentation (such as GPS/GLONASS or GPS/Loran-C), it is possible to quantitatively determine the availability of the augmentation through simulation.

Table 5-1. Integrity Requirements for Supplemental Use of GPS

Phase of Flight	Performance Item			
	Alert Limit	Maximum Allowable Alert Rate	Time to Alarm	Minimum Detection Probability
En Route	2.0 nmi	0.002/Hr	30 seconds	0.999
Terminal	1.0 nmi	0.002/Hr	10 seconds	0.999
Nonprecision Approach	0.3 nmi	0.002/Hr	10 seconds	0.999

The algorithm false detection rate, also referred to as the internal false detection rate, is directly related to availability and continuity. Note that internal detections are transparent to the operator of the positioning system. Once an internal detection occurs, the algorithm immediately selects a different set of measurements, which does not cause a detection. A high internal detection rate causes low continuity (and availability) if only the minimum number of measurements are available. It is desirable to keep the internal false detection rate below the (assumed) true alert rate of the positioning system. The true alert rate of a navigation system is assumed to be on the order of 1e-4 per hour (one true alert per 10,000 hours). It is also assumed that the measurement error correlation time is on the order of two minutes, then it follows that the internal false detection rate should be less than 1e-4/30 or 3.33e-6 on a per sample basis. Therefore, the internal false detection rate for the FDE algorithm was selected as 1e-6 on a per sample basis. Note that the internal false detection rate includes both false and true detections due to normal measurement errors (e.g. receiver noise, propagation uncertainties, selective availability). This is also referred to as fault-free operation.

5.2 Baseline FDE Algorithm

The linearized relation between changes in the measurements and the corresponding change in the user state vector is given by

$$\underline{\delta y} = H\underline{\delta x} \qquad (1)$$

where $\underline{\delta y}$ is a m-by-1 vector containing the changes in the measurements to m sources, $\underline{\delta x}$ is the change in the n-by-1 user state vector, and H is a m-by-n data matrix.

The data matrix H can be decomposed into the product of a real orthonormal matrix Q and an upper triangular matrix R using a "QR" factorization [41],

$$H = QR \qquad (2)$$

Substituting (2) into (1) and pre-multiplying both sides by Q^T yields ($Q^TQ = I$)

$$R\underline{\delta x} = Q^T \underline{\delta y} \qquad (3)$$

The rank of R is equal to the rank of H; therefore, if m > n, the lower m-n rows of R consist of zeros only, and Equation (3) can be divided into two equations

$$U\underline{\delta x} = Q_x^T \underline{\delta y} \quad \text{or} \quad \underline{\delta x} = U^{-1}Q_x^T \underline{\delta y} \qquad (4)$$

$$\underline{0} = Q_p^T \underline{\delta y} \qquad (5)$$

where U consists of the first n rows of R, Q_x^T consists of the first n rows of Q^T, and Q_p^T consists of the last m-n rows of Q^T.

Equation (4) relates the change in the measurements to the change in the user state vector, forming the least squares solution. The rows of Q_p^T and $\underline{\delta y}$ are orthogonal; therefore, the columns of Q_p^T span the parity space of H.

If the measurements are corrupted by errors, then $\underline{\delta y}$ is replaced by $\underline{\delta y} + \underline{e} + \underline{b}$, where $\underline{e}$ is a m-by-1 vector representing zero-mean, normally distributed measurement noise, and $\underline{b}$ is a m-by-1 vector containing bias errors. Normally, $\underline{e}$ and $\underline{b}$ are unknown, but their components in parity space are known from Equation (5):

$$\underline{p} = Q_p^T \underline{e} + Q_p^T \underline{b} \qquad (6)$$

The expected value of the parity vector, $\underline{p}$, is

$$E\{\underline{p}\} = Q_p^T \underline{b} \qquad (7)$$

The covariance matrix of $\underline{p}$ is

$$\text{cov}\{\underline{p}\} = E\{(\underline{p} - E\{\underline{p}\})(\underline{p} - E\{\underline{p}\})^T\} = Q_p^T \,\text{cov}\{\underline{e}\} Q_p \qquad (8)$$

If the measurement noise is uncorrelated and normally distributed with equal variances, then the covariance matrix of the measurement noise is

$$\mathrm{cov}\{\underline{e}\} = \sigma^2 I \qquad (9)$$

where I is a m-by-m identity matrix. It then follows that the covariance matrix of $\underline{p}$ is

$$\mathrm{cov}\{\underline{p}\} = \sigma^2 I \qquad (10)$$

since $Q_p{}^T Q_p = I$ (the rows of Q are orthonormal vectors).

In the absence of bias errors, the parity vector $\underline{p}$ is a function of measurement noise only. In the presence of bias errors, $\underline{p}$ also depends on the bias errors.

5.2.1 One Redundant Measurement

Assume that only one redundant measurement is available, or m = n + 1. In this case, the parity space is one-dimensional and $Q_p{}^T$ is reduced to a row vector (the vector $\underline{q}$ is used to denote the transpose of the first row of $Q_p{}^T$), and the parity vector $\underline{p}$ is reduced to a parity scalar p. In the absence of bias errors, p has a zero-mean normal probability density function given by

$$f_p(x) = \frac{1}{\sigma\sqrt{2x}} e^{-\left(\frac{x}{\sigma\sqrt{2}}\right)^2} \qquad (11)$$

Assume that the failure detection is based on exceeding a detection threshold T_D, then the probability of a false detection is given by

$$P_A = P(|p| > T_D) = \frac{2}{\sigma\sqrt{2x}} \int_{T_D}^{\infty} e^{-\left(\frac{x}{\sigma\sqrt{2}}\right)^2} dx \qquad (12)$$

which can also be written as

$$P_A = \mathrm{erfc}\left(\frac{T_D}{\sigma\sqrt{2}}\right) \qquad (13)$$

where erfc is the complementary error function

$$\mathrm{erfc}(z) = \frac{2}{\sqrt{\pi}} \int_z^{\infty} e^{-\lambda^2} d\lambda \qquad (14)$$

In the presence of a bias error in measurement i only, the parity scalar has a normal distribution with a mean value of

$$\mu_i = \left|\underline{q} \cdot \underline{b}\right| \qquad (15)$$

Only the i^{th} elements of $\underline{q}$ and $\underline{b}$ will contribute to the mean. The probability density function of p is then given by

$$f_p(x) = \frac{1}{\sigma\sqrt{2x}} e^{-\left(\frac{x-\mu_i}{\sigma\sqrt{2}}\right)^2} \qquad (16)$$

Given the detection threshold T_D, the probability of a missed detection is given by

$$P_{MD} = P(|p| \le T_D) = \frac{1}{\sigma\sqrt{2\pi}} \int_{-T_D}^{T_D} e^{-\left(\frac{x-\mu_i}{\sigma\sqrt{2}}\right)^2} dx \qquad (17)$$

When μ_i is positive, an useful upper bound for P_{MD} is given by

$$P_{MD} = P(-T_D < p < T_D) < P(p < T_D)$$

$$P_{MD} < \frac{1}{2}\operatorname{erfc}\left(\frac{\mu_i - T_D}{\sigma\sqrt{2}}\right)$$

when μ_i is negative, a better upper bound is

$$P_{MD} < P(-T_D < p)$$

$$P_{MD} < \frac{1}{2}\operatorname{erfc}\left(\frac{-T_D - \mu_i}{\sigma\sqrt{2}}\right)$$

$$P_{MD} < \frac{1}{2}\operatorname{erfc}\left(\frac{|\mu_i| - T_D}{\sigma\sqrt{2}}\right)$$

thus regardless of the sign of μ_i, we have

$$P_{MD} < \frac{1}{2}\operatorname{erfc}\left(\frac{|\mu_i| - T_D}{\sigma\sqrt{2}}\right) \qquad (18)$$

Equations (13) and (18) provide the performance of the fault detection algorithm in terms of probability of a false detection and probability of a missed detection as a function of:

- Detection threshold T_D;
- Measurement noise standard deviation σ;

- Expected value μ_i of the parity scalar p resulting from a measurement bias error in measurement i.

Obviously, the detection algorithm cannot detect a measurement bias error smaller than the level of measurement noise, since the detection threshold T_D must be set high enough to satisfy the requirement for the false detection probability, see Equation (13).

Given the maximum allowed probability of a detection and the measurement noise standard deviation, an acceptable detection threshold (i.e. one that will be not too likely to cause a detection) is obtained from Equation (13)

$$T_D = \sigma\sqrt{2}\,\mathrm{erfc}^{-1}(P_{FD}) \qquad (19)$$

A detection occurs when the absolute value of the parity scalar exceeds T_D. Next, given the maximum allowed probability of a missed detection, the measurement noise standard deviation and the detection threshold, we may establish μ_M, the minimum detectable absolute expected value of the parity scalar, from Equation (18) as follows:

μ_i is detectable with a high enough probability if

$$|\mu_i| > \mu_M = T_D + \sigma\sqrt{2}\,\mathrm{erfc}^{-1}(2P_{MD}) \qquad (20)$$

Since $\mu_i = \underline{q} \cdot \underline{b}$, Equation (20) implies that the probability of a missed detection is only satisfied if the measurement bias error gives rise to a bias in the parity scalar with absolute value greater than or equal to μ_M. The vector $\underline{q}$ is known from the measurement geometry; therefore, for each measurement i (i = 1 through m), the minimum absolute bias error b_i required to satisfy the probability of a missed detection is calculated from Equation (15).

$$b_i = \frac{\mu_M}{|q_i|} \qquad (21)$$

Combining equations (19), (20), and (21) gives the simple result

$$b_i = \frac{\left(\mathrm{erfc}^{-1}(P_{FD}) + \mathrm{erfc}^{-1}(2P_{MD})\right)\sigma\sqrt{2}}{|q_i|} \qquad (22)$$

In other words, given the probability of a false detection, the probability of a missed detection, and the measurement noise standard deviation, it follows that the minimum detectable measurement bias error is a function of the measurement geometry.

5.2.1.1 Horizontal Radial Position Error

From the probability of a false detection, the probability of a missed detection, the measurement noise standard deviation, and the minimum detectable measurement bias error it is possible to discuss the horizontal radial position error.

Consider the user state error vector resulting from both measurement noise and bias errors. From Equation (4) the user state error vector is

$$\underline{\Delta x} = U^{-1} Q_x^T (\underline{e} + \underline{b}) \qquad (23)$$

The expected value of the user state error vector is

$$E\{\underline{\Delta x}\} = U^{-1} Q_x^T \underline{b} \qquad (24)$$

and the error covariance matrix of $\underline{\Delta x}$ is

$$\mathrm{cov}\{\underline{\Delta x}\} = \sigma^2 \left(U^T U\right)^{-1} \qquad (25)$$

As shown by equations (22) through (24), the effects of the noise and bias errors can be examined separately.

Assume that the vector $\underline{\Delta x}$ is expressed in a locally-level reference frame, then the horizontal components of the expected value and the variance of the user state error vector are given by

$$E\{\underline{\Delta x}_H\} = \begin{pmatrix} \bar{x} \\ \bar{y} \end{pmatrix} \qquad (26)$$

$$\mathrm{var}\{\underline{\Delta x}_H\} = \begin{pmatrix} \sigma^2 \mathrm{XDOP}^2 \\ \sigma^2 \mathrm{YDOP}^2 \end{pmatrix} = \begin{pmatrix} \sigma_x^2 \\ \sigma_y^2 \end{pmatrix} \qquad (27)$$

where: x ,y are the first two components of $E\{\underline{\Delta x}\}$; XDOP^2 and YDOP^2 are the first and second diagonal elements of $(U^T U)^{-1}$, respectively.

First consider the horizontal radial position bias error resulting from measurement bias errors. Each satellite has a minimum bias error necessary for detection with probabilities P_{FD} and P_{MD}, as given by Equation (21). Each of these measurement bias errors can be converted into a horizontal position error using Equation (23) with the other bias components zero. Next, the worst case measurement error is the b_i which maximizes the norm of the horizontal radial position error

$$R_{bias} = \max_i \left(\sqrt{\overline{x_i^{-2}} + \overline{y_i^{-2}}} \right) \qquad (28)$$

The detection algorithm now guarantees that a measurement bias will be detected with the required probabilities P_{FD} and P_{MD} if it contributes to a horizontal radial position error of R_{bias} or greater.

Next, consider the horizontal position error resulting from measurement noise only. The components x and y of the horizontal position error have a bivariate normal probability density function. [42, 43]. Using numerical integration techniques, it is possible to find the radius of a circle which contains a certain percentage of the position solutions. Rather than performing the integration of the bivariate density function directly, the following approximation for the noise radius was found to provide an upper bound for the actual result:

$$R_{noise} = \frac{\sigma\sqrt{2}\,\mathrm{erfc}^{-1}(P_T)\,HDOP}{e^{\left[-0.6050-0.7202\left(\frac{\lambda_1}{\lambda_2}\right)\right]}+1.08} \qquad (29)$$

where: λ_1 and λ_2 are eigenvalues of $(U^T U)^{-1}$; and

$HDOP^2 = XDOP^2 + YDOP^2$.

Note that P_T represents the probability of exceeding an integrity limit, which is on the order of 10^{-7} per flight hour. If the correlation time of the estimated positions is 2 minutes (due to Selective Availability), then P_T on a per sample basis is $10^{-7} / 30 = 3.3 \times 10^{-9}$.

5.2.1.2 Horizontal Integrity Limit (HIL)

To calculate the HIL, two scenarios are considered. Scenario (1): in the absence of measurement bias errors, the noise protection radius is approximated by Equation (29), using a value on the order of 3.3×10^{-9} for P_T. Scenario (2): in the presence of both measurement noise and a measurement bias error, the bias protection radius as calculated by Equation (28) is used. Because it is not known which scenario exists, the fault detection algorithm must use the largest of the two protection radii calculated for the two scenarios. In general, the HIL is driven by Equation (28).

The selection of Equation (28) for Scenario (2) is justified as follows. If a measurement error exists such that the worst case bias is achieved, then the probability of a missed detection in parity space is P_{MD}. However, due to measurement noise, the actual position error could be either inside or outside R_{bias}. Therefore, the probability of a missed detection in position space (loss of integrity) is approximately $0.5*P_{MD}$. For this case, the HIL is conservative, and could be improved by recalculating the HIL using $2*P_{MD}$. Unfortunately, this would increase the probability of a missed detection in position space if the bias error is around 0.7 to 0.8 of its worst case value. It was found by simulation that Equation (28) is a good approximation for the calculation of the HIL.

Further note that P_{MD} is the probability of a missed detection for the fault detection algorithm. The probability of loss of integrity is the product of the probability that a fault exists and the probability of a missed detection given that a fault exists.

5.2.2 Two Redundant Measurements

If two redundant measurements are available, or m = n + 2, the parity vector contains two elements. The norm of the parity vector is now used as the detection statistic. The norm of the parity vector squared has two-degrees-of-freedom (2 DOF) chi-square properties.

A similar procedure is used as for the case of one redundant measurement. First, the detection threshold, T_D, is calculated such that the probability of false detection is 3.3e-7. Next, the minimum detectable bias is calculated which is needed to satisfy the probability of detection of 0.999. This is followed by the calculation of the HIL.

The normalized (σ=1) 2 DOF chi-square density function is given by

$$f_x(x) = 0.5e^{-0.5x} \qquad (30)$$

The area under the tail of the density function is to be P_{FD}. Therefore

$$P_{FD} = \int_{T_D^2}^{\infty} 0.5e^{-0.5x}\,dx \qquad (31)$$

$$\text{or } T_D = \sqrt{-2 \cdot \ln(P_{FD})}$$

Using a P_{FD} = 3.3e-7, T_D = 5.46. This is the normalized threshold that is used if the magnitude of the parity vector is used as the test statistic. If the threshold is not normalized, then the threshold must be multiplied by the standard deviation of the measurement noise. (e.g. if σ = 33 m and the magnitude of the parity vector is the test statistic, T_D = 33 x 5.46 = 180.2 m).

The minimum detectable bias is calculated using the normalized 2 DOF noncentral chi-square density function given by

$$f_{\aleph}(x) = 0.5e^{-0.5(x+\mu_M^2)} \sum_{j=0}^{\infty} \frac{x^j (\mu_M^2)^j}{2^{2j}\, j!\, j!} \qquad (32)$$

where μ_M is the noncentrality parameter.

The desired missed detection probability is obtained by integrating Equation (32) from zero to the detection threshold squared.

Note that μ_M is a function of the number of satellites in view; but, for a given m, it does not vary with the satellite geometry.

Recall that a bias error in measurement i has components along the axes in parity space given by column i of Q_p^T. Each column of Q_p^T defines a measurement axis in parity space: an error in measurement i will lie along the i^{th} measurement axis in parity space. Therefore, a measurement range bias is transformed into a bias in the parity vector by multiplying the range bias by the norm of column i of Q_p^T.

The minimum absolute bias error, b_i, required to satisfy the probability of missed detection is calculated from

$$b_i = \frac{\mu_M}{|\underline{m}_i|} \qquad (33)$$

where $\underline{m}_i$ is the i^{th} column of Q_p^T.

Similar to the case of one redundant measurement, the HIL is calculated from equations (28) and (29).

5.2.3 Fault Exclusion

Rather than performing fault isolation, fault exclusion is used. The baseline algorithm will select the best set of n+2 measurements (best in terms of smallest HIL). If only n+1 measurements are available, then the algorithm will use these n+1 measurements. If a detection occurs, the algorithm will select the next best set of n+2 measurements that will have a detection statistic that is less than half of the detection threshold, T_D, and a HIL that is less than the alert limit. If no sub-set exists that has a detection statistic that is less than $0.5*T_D$, the sub-set with the smallest detection statistic is selected, provided that it is still less than T_D. In the case of n+1 measurements, fault exclusion is not possible.

5.2.4 Unequal RMS Error Levels

So far, all measurements were assumed to have the same statistics. If this is not the case, then the FDI algorithm is modified as follows to incorporate a measurement error covariance matrix. To accommodate different measurement variances, Equation (1) is left multiplied by a weighting matrix W [44]

$$W\underline{\delta y} = WH\underline{\delta x} \qquad (34)$$

The "QR" factorization is now performed on WH and Equation (3) is replaced by

$$R\underline{\delta x} = Q^T W\underline{\delta y} \qquad (35)$$

and the parity vector is now obtained from

$$\underline{p} = Q_p^T W \underline{\delta y} \qquad (36)$$

In general, W could be derived from the measurement noise covariance matrix, but in most applications it is sufficient to simply use a diagonal matrix, where the diagonal elements are the inverses of the measurement noise standard deviations. If W is correctly selected, then the elements of $W\underline{\delta y}$ have unit standard deviation. The introduction of the weighting matrix also simplifies the calculation of the detection threshold, since this calculation is now independent of the measurement noise standard deviation.

6.0 SUMMARY OF RESEARCH RESULTS

Major findings of the research described in this report are:

1) Feasibility demonstration in October of 1994 of a carrier-smoothed code-phase differential GPS system for Category IIIB (autoland) applications through flight-testing on a Boeing-757 aircraft operated by the United Parcel Service; [1 – 4]

2) Successful flight-test demonstration of a prototype LAAS for Category III landings at the William J. Hughes Technical Center in Atlantic City using FAA's Boeing 727. The architecture of this system forms the basis for the next generation of GPS-based aircraft landing systems. [5 - 10]

Other significant findings include:

1) Feasibility demonstration of hybrid DGPS/ILS Glide Slope for aircraft precision approach and landing on a Boeing-757 aircraft. [2]
2) Design and implementation of an integrated multipath-limiting antenna (IMLA) system to significantly reduce the error due to ground multipath. [9, 10, 18]
3) Successful demonstration of the use of the Very-High Frequency (VHF) data broadcast (VDB) system for LAAS. [11]
4) Flight test demonstration of low-cost inertial aiding of differential GPS with coasting time periods of up to two seconds, while maintaining centimeter-level accuracy. [12]
5) Demonstrated feasibility of using a sophisticated simulator to test and characterize high-accuracy differential GPS architectures. [13]
6) Completion of computer models to investigate the availability, integrity and coverage of differential GPS architectures. [8, 15]
7) Completion of a ground multipath model to predict and analyze the effect of earth-surface-based multipath. The model was used to design the IMLA system. [17]
8) Characterization of pseudolite multipath error using an off-frequency pseudolite architecture. [18]
9) First successful integration of an on-airport pseudolite into the LAAS to achieve sub-meter pseudolite ranging accuracy. [19, 20]
10) Major contributions to the development and testing of fault detection and exclusion (FDE) techniques for GPS augmentations, including the development of a baseline FDE algorithm and test procedures. [21 - 23]

7.0 REFERENCES

1. Waid, James D., "Design of a DGPS Ground Station," M.S.E.E. Thesis, School of Electrical Engineering and Computer Science, Ohio University, 1993.

2. Van Graas, F., D. Diggle, V. Wullschleger, R. Velez, G. Kuehl, R. Hilb, and M. Dimeo, "FAA/Ohio University/UPS Autoland Flight Test Results," Proceedings of the National Technical Meeting of The Institute of Navigation, January 1995, Anaheim, CA.

3. Braff, R., P. O'Donnell, V. Wullschleger, C. Mackin, R. Velez, R. Swider, P. Enge, D. Kaufmann, F. van Graas, "FAA's CAT III Feasibility Program: Status and Accomplishments," Proceedings of the ION GPS-95 Meeting, Palm Springs, CA, September 1995.

4. Van Graas, F., D. Diggle, M. Uijt de Haag, V. Wullschleger, R. Velez, D. Lamb, M. Dimeo, G. Kuehl, and R. Hilb, "FAA/Ohio University/United Parcel Service DGPS Autoland Flight Tests Demonstration," Proceedings of the ION GPS-95 Meeting, Palm Springs, CA, September 1995.

5. Shane-Woei Lee, "On-The-Fly Carrier Phase Ambiguity Resolution Without Using Pseudorange Measurements For Satellite-Based Differential Positioning," M.S.E.E. Thesis, School of Electrical Engineering and Computer Science, Ohio University, 1994.

6. Van Graas, F. and S. W. Lee, "High-Accuracy Differential Positioning for Satellite-Based Systems Without Using Code-Phase Measurements," Proceedings of the National Technical Meeting of The Institute of Navigation, January 1995, Anaheim, CA.

7. Van Graas, F. and S. W. Lee, "High-Accuracy Differential Positioning for Satellite-Based Systems Without Using Code-Phase Measurements," NAVIGATION: Journal of The Institute of Navigation, Vol. 42, No. 4, Winter 1995-1996.

8. Liu, F., T. Skidmore, and F. van Graas, "Ohio University LAAS Monitoring: Design and Performance," Proceedings of the ION GPS-96 Meeting, Kansas City, Missouri, September 1996.

9. Van Graas, F., D.W. Diggle, T. Skidmore, M. Uijt de Haag, M.F. DiBenedetto, V. Wullschleger, and R. Velez, "Ohio University/FAA Flight Test Demonstration Results of the Local Area Augmentation System (LAAS)," Proceedings of the ION GPS-97 Meeting, Kansas City, Missouri, September 1997.

10. Van Graas, F., D.W. Diggle, T. Skidmore, M. Uijt de Haag, M.F. DiBenedetto, V. Wullschleger, and R. Velez, "Ohio University/FAA Flight Test Demonstration

Results of the Local Area Augmentation System (LAAS)", NAVIGATION: Journal of The Institute of Navigation, 1998.

11. Skidmore, T., F. van Graas, and M. Uijt de Haag, "Flight Test Results of the LAAS Navigation Augmentation Broadcast System," Proceedings of the ION GPS-97 Meeting, Kansas City, Missouri, September 1997.

12. Mathur, Navin, "Feasibility of Using a Low-Cost Inertial Measurement Unit with Centimeter Accuracy Differential Global Positioning System," Ph.D. Dissertation, School of Electrical Engineering and Computer Science, Ohio University, 1999.

13. Van Graas, F., D. Diggle, L. Lake, and S. Newman, "Laboratory Testing of an Interferometric GPS Flight Reference System," Proceedings of the 51st Annual Meeting of The Institute of Navigation, 5-7 June 1995, Colorado Springs, CO.

14. Van Graas, F. and T. Skidmore, "GPS Integrity Monitoring and Multipath Error Distributions," Proceedings of the 49th Annual Meeting of The Institute of Navigation, Cambridge, MA, June 22, 1993.

15. Mohammed Shaltot, "Availability Studies for the GPS," M.S.E.E. Thesis, School of Electrical Engineering and Computer Science, Ohio University, 1993.

16. Van Graas, F. and T. Skidmore, "DGPS Ground Station Integrity Monitoring," Proceedings of the 1994 National Technical Meeting of The ION, San Diego, CA, January 1994.

17. Aloi, D. "Electromagnetic Analysis of Ground Multipath for Satellite-Based Positioning Systems," M.S.E.E. Thesis, School of Electrical Engineering and Computer Science, Ohio University, 1996.

18. Bartone, C. and F. van Graas, "Airport Pseudolite Subsystem for the Local Area Augmentation System," Proceedings of the ION GPS-97 Meeting, Kansas City, Missouri, September 1997.

19. Bartone, C. and F. van Graas, "Airport Pseudolites for Local Area Augmentation," Proceedings of IEEE PLANS '98 Position Location and Navigation Symposium, Palm Springs, CA, April 1998.

20. Chris Bartone, "Ranging Airport Pseudolite for Local Area Augmentation Using the Global Positioning System," Ph.D. Dissertation, School of Electrical Engineering and Computer Science, Ohio University, 1998.

21. Farrell, J. L. and F. van Graas, "Statistical Validation for GPS Integrity Test," NAVIGATION: Journal of The Institute of Navigation, Vol. 39, No.2, Summer 1992.

22. Farrell, J. L. and F. van Graas, "Integrity Testing for GNSS Sole Means," Proceedings of the 1994 National Technical Meeting of The ION, San Diego, CA, January 1994.

23. Farrell, J. L. and F. van Graas, "Baseline Fault Detection and Exclusion Algorithm," Proceedings of the 49th Annual Meeting of The Institute of Navigation, Cambridge, MA, June 22, 1993.

24. Swider, R., "FAA LAAS Architecture," presented at ICAO GNSSP meeting, Gold Coast, Australia, 1997.

25. Van Dierendonck, A. J., et al., "Proposed Airport Pseudolite Signal Specification for GPS Precision Approach Local Area Augmentation Systems," Proceedings of ION GPS-97, The Satellite Division of The Institute of Navigation, Kansas City, Missouri, 16-19 September 1997.

26. Braff, R., "Description of the FAA Local Area Augmentation System (LAAS)," MITRE Technical Report MTR 97W0000076, The MITRE Corporation, McLean, Virginia, December 1997.

27. Moelker, D-J., "Multiple Antennas for Multipath Direction Finding and GNSS Multipath Mitigation," Proceedings of ION GPS-97, The Satellite Division of The Institute of Navigation, Kansas City, Missouri, 16-19 September 1997.

28. Braasch, M. S., "GPS Multipath Model Validation," Proceedings of PLANS'96, IEEE Aerospace and Electronic Systems Society, Atlanta, GA, April 1996.

29. Braasch, M. S., "Optimum Antenna Design for DGPS Ground Reference Stations," Proceedings of ION GPS-94, The Satellite Division of The Institute of Navigation, September 1994.

30. Liu, F., et al., "LAAS Signal-in-Space Integrity Monitoring Description and Verification Plan," Proceedings of ION GPS-97, The Satellite Division of The Institute of Navigation, Kansas City, Missouri, 16-19 September 1997.

31. Farrell, J. L., "Radical Streamlining of GPS/INS," Proceedings of the 11th International Technical Meeting of the Satellite Division of the Institute of Navigation, ION GPS-98, Sept. 1998.

32. Harrington, R. L., and Dolloff, J. T., "The Inverted Range: GPS User Test Facility," Proceedings, IEEE Position, Location, and Navigation, Symposium, (PLANS) 1976, IEEE New York, Nov. 1976, pp. 204-211.

33. B. Winer, et al., "GPS Receiver Laboratory RFI Tests," Proceedings from the Institute of Navigation-GPS-96, January 1996, pp. 674-675.

34. Van Graas, F. “GNSS Augmentation for High Precision Navigation Services”, Advisory Group for Aerospace Research & Development-Lecture Series 207, June 1996, pp. 8-1 to 8-3.

35. RTCA SC-159, “Proposed Wideband Pseudolite Interface Control Document,” September 1998.

36. Wilcox, J.C., “Competitive Evaluation of Failure Detection Algorithms for Strapdown Redundant Inertial Instruments,” Journal of Spacecraft and Rockets, Vol. 11, July 1974.

37. Gai, E.G., Adams, M.B. and Walker, B.K., “Determination of Failure Thresholds in Hybrid Navigation,” IEEE Transactions on Aerospace and Electronic Systems, Vol. AES-12, November 1976.

38. Daly, K.C., Gai, E.G. and Harrison, J.V., “Generalized Likelihood Test for FDI in Redundant Sensor Configurations,” Journal of Guidance and Control, Vol. 2, January-February 1979.

39. Potter, J.E. and Suman, M.C., “Thresholdless Redundancy Management with Arrays of Skewed Instruments,” Integrity in Electronic Flight Control Systems, AGARDOGRAPH-224, 1977.

40. Sturza, M., “Navigation System Integrity Monitoring Using Redundant Measurements,” NAVIGATION: Journal of the Institute of Navigation, Vol. 35, No. 4, Winter 1988-89.

41. Golub, G.H. and Van Loan, C.F., “Matrix Computations,” Second Edition, The Johns Hopkins University Press, Baltimore, MD, 1989.

42. Torrieri, D.J., “Statistical Theory of Passive Location Systems,” IEEE Transactions on Aerospace and Electronic Systems, Vol. AES-20, March 1984.

43. Chin, G.Y., “Two-Dimensional Measures of Accuracy in Navigational Systems,” Final Report, No. DOT-TSC-RSPA-87-1, U.S. DOT, NVTSC, March 1987.

44. Lawson, C.L. and Hanson, R.J., “Solving Least Squares Problems,” Prentice-Hall, Inc., Englewood Cliffs, New Jersey, 1974.